

# A generalized “reaction–diffusion” model to describe spatio-temporal patterns in the catalytic CO oxidation on Pt(110)

José Verdasca,<sup>a,b</sup> Pierre Borckmans<sup>\*b</sup> and Guy Dewel<sup>b</sup>

<sup>a</sup> Centro de Física da Matéria Condensada, Av. Prof. Gama Pinto, 2, P-1649-003 Lisboa, Portugal. E-mail: verdasca@alf1.cii.fc.ul.pt

<sup>b</sup> Service de Chimie-Physique C.P. 231, Université Libre de Bruxelles, 1050 Bruxelles, Belgium. E-mail: pborckm@ulb.ac.be

Received 15th October 2001, Accepted 5th February 2002

First published as an Advance Article on the web 19th March 2002

A macroscopic model to describe the spatio-temporal patterns observed in the CO + O<sub>2</sub> reaction on Pt(110) is presented. We consider mass transport in the adsorbed layer as a response to the gradient in chemical potential of adsorbed CO and explicitly take into account the coupling between diffusion and the adsorbate-induced structural transformation of the substrate. Numerical integration of the model equations in two-dimensions revealed target patterns, spiral waves as well as subharmonic standing-wave patterns that closely resemble those observed in experiments. Our results also show that synchronization of the surface can be achieved through nucleation and growth processes even in the absence of gas-phase coupling.

## I. Introduction

A wide variety of complex spatiotemporal phenomena has been observed in heterogeneously catalyzed reactions.<sup>1</sup> So far, the richest collection of spatiotemporal patterns observed was obtained in the CO oxidation on the Pt(110) single crystal surface, under isothermal and ultra-high vacuum conditions. Depending on the values of the control parameters – the temperature  $T$ , as well as the CO and O<sub>2</sub> partial pressures – patterns such as propagating reaction fronts, spiral waves, targets, standing waves, oscillating cellular structures and chemical turbulence have been observed.<sup>2–7</sup>

Before these spatial features could be resolved, the average temporal features were already under scrutiny for some time. Work function measurements revealed regular as well as chaotic oscillations in the average surface coverages of the two reacting species and in the rate of CO<sub>2</sub> production.<sup>8–10</sup>

The mechanism underlying the oscillations has been clearly established:<sup>10–12</sup> the most stable phase of the clean Pt(110) surface is reconstructed, exhibiting the so-called “missing-row” structure, in which every second row in the [110] direction is lacking (Fig. 1). It is denoted 1 × 2 after its crystallographic signature. Within a certain temperature range, the adsorption of CO lifts the reconstruction, that is, causes the surface to revert to the termination of the fcc bulk structure – the 1 × 1 square arrangement. As oxygen adsorption is enhanced on the 1 × 1 surface,<sup>13</sup> an autocatalytic loop is formed that is responsible for oscillations.

Based upon this mechanism, a kinetic model was proposed that could reproduce well the *regular* oscillatory behaviour of the CO + O<sub>2</sub> reaction on Pt(110).<sup>14</sup> The KEE model, as it became known, consists in a set of three coupled ODEs describing the evolution of the average surface coverage of adsorbed CO (CO<sub>ad</sub>) and oxygen (O<sub>ad</sub>) as well as the behaviour of a third variable representing the ratio of the surface in the 1 × 1 configuration.

However successful in reproducing regular oscillations, the KEE model displays a low-dimensional chaotic attractor only for unrealistic values of the parameters. This finding reinforced

the belief, already suggested by previous experiments,<sup>8</sup> that chaotic behaviour of average rates was connected to underlying turbulent spatio-temporal patterns. In order to display chaotic behaviour, the dynamical system had to acquire infinite degrees of freedom through spatial coupling. Thereupon, spatial effects were accounted for merely by adding to the system of ODEs a linear Fickian diffusion term for CO<sub>ad</sub>,<sup>15</sup> oxygen sticking so strongly to the surface that it can in practice be considered as immobile. This approach was clearly inspired by the successful modelling of spatio-temporal phenomena in chemical reactions in solution, such as the Belousov–Zhabotinski reaction.

In heterogeneous catalysis though, oscillations do not take place in a dilute medium. On the contrary, in most situations the couple adsorbate–substrate exhibits typical properties of

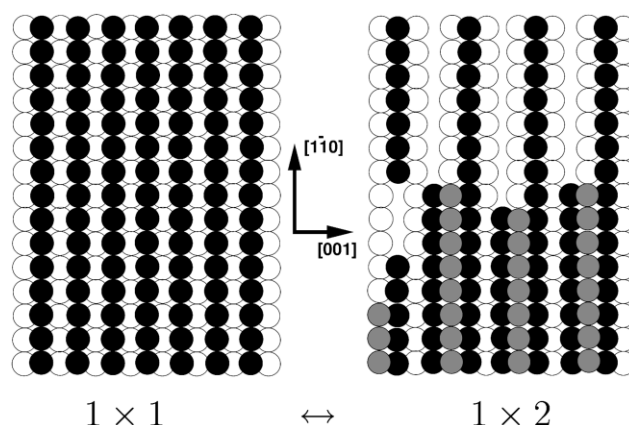


**Fig. 1** Ball model illustrating the 1 × 1 ↔ 1 × 2 surface phase transition of the Pt(110) surface. The “missing-row” structure shown on the right is created by removing (partially) every second row in the top part of the 1 × 1 structure on the left and then placing the displaced atoms (shown in grey) on top of the rows in the lower half of the surface.

a condensed system, like the structural phase transition (SPT) of the Pt(110) surface in the present case. Moreover, at least during a part of the oscillation cycle, the adsorbed layer is quite densely packed. Thus, the effects of adsorbate–adsorbate interactions and/or site competition between reactants cannot be neglected.

The CO oxidation on Pt(110) is a striking example of non-ideal behaviour in transport processes during a catalytic reaction. Because the SPT of the substrate plays such a fundamental role in the oscillatory mechanism, there must be strong implications to mass transport in the adlayer which are unaccounted for in the traditional reaction–diffusion approach. Since the  $\text{CO}_{\text{ad}}-1 \times 1$  configuration is energetically preferred to CO adsorbed on the  $1 \times 2$  phase, diffusion of CO molecules from  $1 \times 2$ -regions to  $1 \times 1$ -regions must be strongly enhanced. Following CO adsorption on the  $1 \times 2$  phase, a rapid  $1 \times 2 \rightarrow 1 \times 1$  conversion causes the nucleation and growth of  $\text{CO}_{\text{ad}}-1 \times 1$  patches, which subsequently act as traps for CO molecules migrating on adjacent reconstructed domains.

A first attempt to incorporate analogous features in a model of an heterogeneous catalyzed reaction was made by Tammaro and Evans,<sup>16</sup> but for the CO-oxidation on Pt(100). They regarded the adsorbate–substrate system as a percolating network and analyzed the propagation of reactive pulses in that perspective.

Here we take a somewhat different, more general, approach and consider mass transport in the adsorbed layer as a global response to a gradient in the chemical potential of the mobile adspecies, not simply to the concentration gradient as assumed in Fick's first law. In this “nucleation and growth” mechanism, from the metastable  $1 \times 1$  nuclei created in a first step – where CO coverage is high – some grow to larger domains at the expense of the evaporation of smaller islands. This process is simply the manifestation of Ostwald ripening in the present context. It leads to a distribution of CO-rich and CO-poor regions in the adsorbed layer, where the reaction with oxygen takes place with different probabilities. Ultimately, it provides a powerful mechanism of synchronization over long distances that is responsible for the establishment of spatio-temporal patterns.

Such a strong spatial coupling cannot arise from Fickian diffusion, as clearly demonstrated by the fact that the KEE model supplemented with a Fickian term is unable to produce robust spatio-temporal patterns.<sup>15</sup> Therefore it was reckoned that spatial coupling alone could not give rise to synchronized behaviour in the CO oxidation on Pt(110) and since then its occurrence has been mainly attributed to the action of gas-phase coupling.<sup>1,6,15,17,18,19</sup>

However, the notion that global coupling through the gas phase is a necessary ingredient for coherent spatio-temporal pattern formation in this reaction has been challenged by Monte Carlo simulations.<sup>20</sup> These studies also stressed the crucial role played by nucleation and growth processes in the establishment of synchronized behaviour on the  $\text{CO} + \text{O}_2/\text{Pt}(110)$  system. Notwithstanding, the ability of MC simulations to provide a basis for the interpretation of experimental results is strongly limited by the fact that the number of particles involved is too small.

So, here we go back to a macroscopic description in terms of generalized mass balance equations,<sup>21</sup> which consistently incorporates the coupling between diffusion in the adlayer and the SPT through a nonlinear transport term. As we shall see, the model we propose is able to reproduce the main qualitative features of the observed spatio-temporal patterns, including their symmetry.

The present manuscript is organized as follows. In section II, we introduce the generalized “reaction–diffusion” model that stems from the conceptual framework briefly outlined above. In sections III and IV, we present and discuss numerical results, respectively in one and two dimensions. Section V is

reserved for a discussion of the approach devised here, in parallel with the role of gas-phase coupling. A brief conclusion (section VI) ends the paper.

## II. The model

An adsorbate-induced phase transition of a metal surface is a very complex phenomenon that nevertheless can be qualitatively modelled with great simplicity as a first order transition in the framework of the lattice-gas.<sup>22</sup> In the mean-field approximation, the total free energy density of the couple adsorbate–surface is a sum of three contributions

$$f = f_{\text{ad}} + f_{\text{s}} + f_{\text{int}}, \quad (2.1)$$

where  $f_{\text{ad}}$  is the free energy density of adsorbed particles

$$f_{\text{ad}} = -E^{1 \times 2} \theta + \varepsilon \theta^2 / 2 + RT[\theta \ln \theta + (1 - \theta) \ln (1 - \theta)], \quad (2.2)$$

$f_{\text{s}}$  the free energy of surface atoms:

$$f_{\text{s}} = \Delta E \kappa + RT[\kappa \ln \kappa + (1 - \kappa) \ln (1 - \kappa)], \quad (2.3)$$

and  $f_{\text{int}}$  the interaction energy responsible for the stabilization of the otherwise metastable  $1 \times 1$  phase:

$$f_{\text{int}} = -\alpha \theta \kappa. \quad (2.4)$$

$\theta$  is the adsorbate coverage and  $\kappa$  the percentage of surface in the  $1 \times 1$  phase. Furthermore,  $-E^{1 \times 2}$  is the adsorption energy in the  $1 \times 2$  phase while  $\Delta E$  is the energy difference *per surface atom* between the clean  $1 \times 1$  and  $1 \times 2$  surfaces. Finally,  $\varepsilon$  is the energy of lateral interaction between adparticles and  $\alpha$  an adsorbate–surface interaction energy parameter.

The fact that, as shown in Fig. 2, for temperatures below the critical temperature  $T < T_c$  and for suitable choices of the energetic parameters –  $\Delta E$  and  $\alpha$  – the equilibrium chemical potential

$$\mu_{\text{eq}}(\theta) = -E^{1 \times 2} + \varepsilon \theta + RT \ln[\theta/(1 - \theta)] - \frac{\alpha}{1 + \exp[(\Delta E - \alpha \theta)/RT]}, \quad (2.5)$$

is a non-monotonous function of coverage, provides the unequivocal signature of a phase transition. For  $T < T_c$ , even in the case of repulsive adsorbate–adsorbate interactions ( $\varepsilon > 0$ ), a system with initial homogeneous coverage within the range of thermodynamic instability, will spontaneously

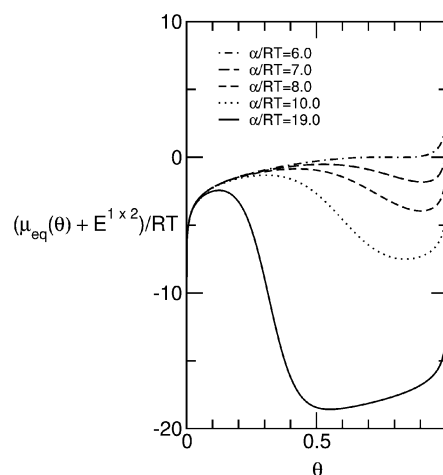


**Fig. 2** Shape of the equilibrium chemical potential as the parameter  $\alpha/RT$  varies at fixed  $\Delta E/RT = 6.0$  and  $\varepsilon = 0$ . Note the existence of a second-order transition at  $\alpha/RT \approx 6.0$ .

separate into high and low coverage domains driven solely by adsorbate–substrate interactions.

The free energy eqns. (2.2)–(2.4) can be straightforwardly extended to a ternary mixture composed of adsorbed CO molecules and O atoms *plus* the unoccupied adsorption sites. The contribution from the adlayer reads then

$$f_{\text{ad}} = -E_{\text{CO}}^{1 \times 2} \theta_{\text{CO}} - E_{\text{O}}^{1 \times 2} \theta_{\text{O}} + RT[\theta_{\text{CO}} \ln \theta_{\text{CO}} + \theta_{\text{O}} \ln \theta_{\text{O}} + (1 - \theta_{\text{CO}} - \theta_{\text{O}}) \ln(1 - \theta_{\text{CO}} - \theta_{\text{O}})], \quad (2.6)$$

where  $E_{\text{CO}}^{1 \times 2}$  ( $E_{\text{O}}^{1 \times 2}$ ) is the CO (oxygen) adsorption energy in the reconstructed phase, and  $\theta_{\text{CO}}$  and  $\theta_{\text{O}}$  are the coverages of the co-adsorbed species. On Pt(110), adsorbed oxygen does not affect the surface structure, *i.e.* it does not induce reconstruction of the  $1 \times 1$  surface nor destabilize the reconstructed  $1 \times 2$  phase.<sup>13,23</sup> Therefore, the interaction energy is simply

$$f_{\text{int}} = -\alpha \theta_{\text{CO}} \kappa. \quad (2.7)$$

Notice that on writing (2.6) we neglected interadsorbate interactions. In what follows we will focus exclusively on the effect of the adsorbate-induced SPT (*i.e.* we take  $\varepsilon = 0$ ).

In order to account for spatial inhomogeneities varying in a very long scale compared to interlattice spacing, a free energy functional is constructed by adding to the free energy density (2.1), with terms on the r.h.s. given by (2.3), (2.6) and (2.7), the contributions due to coverage gradients up to first order, then integrating over the whole surface area:

$$\mathcal{F}\{\theta_{\text{CO}}, \theta_{\text{O}}, \kappa\} = \int \text{d}\mathbf{r} \left[ f(\theta_{\text{CO}}, \theta_{\text{O}}, \kappa) + \frac{\gamma}{2} (\nabla \theta_{\text{CO}})^2 \right]. \quad (2.8)$$

Above, the assumption was made that the contribution from CO coverage gradients dominates over all other possible contributions of the same sort, respecting the same symmetries. It can be justified by the leading role played by migration and trapping of CO molecules on  $1 \times 1$  regions, in the process that leads to the formation of interfacial boundaries. Moreover, the adsorption of CO is solely responsible for triggering the phase separation and besides, CO is the only mobile species present on the surface. Indeed, in the temperature range where the effects we wish to describe were observed, the oxygen mobility is so low that it may be neglected.

The mass current flow of adsorbed CO,  $\mathbf{J}_{\text{CO}}$ , is the gradient of the chemical potential:

$$\mathbf{J}_{\text{CO}} = -M \nabla \mu_{\text{CO}}, \quad (2.9)$$

where

$$\mu_{\text{CO}} = \frac{\delta \mathcal{F}\{\theta_{\text{CO}}, \theta_{\text{O}}, \kappa\}}{\delta \theta_{\text{CO}}}, \quad (2.10)$$

and  $M$  is the mobility of adsorbed CO, supposedly constant. The mass balance equation for the surface coverage of CO then takes the following form:

$$\frac{\partial \theta_{\text{CO}}}{\partial t} = Kn^{\text{CO}}\{\theta_{\text{CO}}, \theta_{\text{O}}\} - \nabla \mathbf{J}_{\text{CO}}. \quad (2.11)$$

Spatial derivatives are absent from the evolution equation for  $\theta_{\text{O}}(\mathbf{r}, t)$ ; thus,

$$\frac{\partial \theta_{\text{O}}}{\partial t} = Kn^{\text{O}}\{\theta_{\text{CO}}, \theta_{\text{O}}, \kappa\}. \quad (2.12)$$

The kinetic terms  $Kn^{\text{CO}}$  and  $Kn^{\text{O}}$ , accounting for the exchange processes between the adsorbed layer and the gas phase are essentially those in the KEE model,<sup>14</sup> apart from the minor simplification of having both saturation coverages set to unity:

$$Kn^{\text{CO}} = p_{\text{CO}} s_{\text{CO}} k_{\text{CO}} (1 - \theta_{\text{CO}}^r) - k_{\text{d}} \theta_{\text{CO}} - k_{\text{r}} \theta_{\text{CO}} \theta_{\text{O}}, \quad (2.13)$$

$$Kn^{\text{O}} = p_{\text{O}_2} s_{\text{O}} k_{\text{O}_2} (1 - \theta_{\text{CO}} - \theta_{\text{O}})^2 - k_{\text{r}} \theta_{\text{CO}} \theta_{\text{O}}. \quad (2.14)$$

The three terms in the r.h.s. of eqn. (2.13) describe respectively CO adsorption, CO desorption and the oxidation reaction through the Langmuir–Hinshelwood mechanism. CO adsorbs through a precursor state without adsorption site inhibition from pre-adsorbed oxygen. The effect of precursor adsorption is accounted for by the exponent  $r > 1$ , in eqn. (2.13).<sup>24</sup> Oxygen adsorption is dissociative, thus second order on the number of empty sites. Furthermore, there is no desorption term in eqn. (2.14) because at the temperatures considered here the rate at which strongly bounded oxygen leaves the surface is so low that it can be neglected.  $k_{\text{CO}}$  and  $k_{\text{O}_2}$  are the rates at which respectively CO and  $\text{O}_2$  hit the surface at unit pressure, whereas  $k_{\text{d}}$  and  $k_{\text{r}}$  are, in the order mentioned, the desorption and reaction rate constants. These are described by Arrhenius laws where the values of the pre-exponential factors and activation energies have been determined in several experiments and are comprehensively listed in ref. 14.

Oscillations are not predicted by eqns. (2.11) and (2.12) alone; the structural transformation of the substrate must be taken into account also. Like in ref. 14, the coupling between a third equation ruling the dynamics of the SPT and the evolution equations for the coverages – eqns. (2.11) and (2.12) – is achieved through the dependence of the oxygen sticking coefficient on the state of the surface, that is on the variable  $\kappa$ , by writing

$$s_{\text{O}}(\kappa) = s_{\text{O}}^{1 \times 1} \kappa + s_{\text{O}}^{1 \times 2} (1 - \kappa), \quad (2.15)$$

where  $s_{\text{O}}^{1 \times 1}$  and  $s_{\text{O}}^{1 \times 2}$  are respectively the sticking coefficients in the  $1 \times 1$  and  $1 \times 2$  phases. We take  $s_{\text{O}}^{1 \times 1}/s_{\text{O}}^{1 \times 2} = 2$  which in a context where the  $[1\bar{1}0]$  atomic rows are identified as the active sites for initial adsorption and dissociation of molecular oxygen, must be considered as a theoretical upper limit. Nevertheless this value agrees well with the few experimental results which do suggest that the  $1 \times 1$  surface is almost twice as active as the  $1 \times 2$  with respect to oxygen adsorption.<sup>13</sup> In ref. 14 a smaller ratio of  $s_{\text{O}}^{1 \times 1}/s_{\text{O}}^{1 \times 2} = 1.5$  was used. Yet, we found that the difference did not affect qualitatively the outcome of the simulations and so, for clarity purposes, we preferred to use the integer value. On the other hand, the sticking coefficient for CO adsorption,  $s_{\text{CO}}$ , is unity.

The equation describing the relaxation of the surface structure, hence the local evolution of  $\kappa(\mathbf{r}, t)$ , must reflect the fact that the surface is able to entirely switch from one atomic arrangement to another without constraint, namely in the form of a conservation law. As it is clear from Fig. 1, even though the number of Pt atoms is conserved, the area of either surface arrangement is not. The displaced atoms form a terrace in the  $1 \times 2$  configuration over the  $1 \times 1$  surface leaving those portions of the surface where they used to sit *also* in the  $1 \times 2$  configuration. We can think of the reverse process,  $1 \times 2 \rightarrow 1 \times 1$ , as those atoms being returned to their original positions. Of course, the microscopic roughening of the surface due to the build up of numerous terrace layers one atom high cannot be described by our mean-field model. We just suppose there will be regions where the average density of reconstructed patches largely surmounts the portions of the surface displaying a  $1 \times 1$  arrangement – low  $\kappa$  regions – and that elsewhere on the surface, at the same time, exactly the opposite is happening – high  $\kappa$  domains. Like the coverages,  $\kappa$  is a coarse grained variable. It must be interpreted as the local area fraction of the  $1 \times 1$  phase averaged over a domain of linear size  $R_{\text{D}}$  much larger than the interlattice spacing  $a$ ,  $R_{\text{D}} \gg a$ .

In other words,  $\kappa(\mathbf{r}, t)$  is a non-conserved order parameter and its dynamics is purely relaxational.<sup>25</sup> Accordingly, we write:



$$\frac{\partial \kappa}{\partial t} = -L \frac{\delta \mathcal{F} \{ \theta_{\text{CO}}, \theta_{\text{O}}, \kappa \}}{\delta \kappa} = -L \left[ \Delta E + RT \ln \left( \frac{\kappa}{1-\kappa} \right) - \alpha \theta_{\text{CO}} \right], \quad (2.16)$$

where  $L$  is a constant fixing the time scale of the reconstruction process.

It is insightful to make a parallel with the theory of phase-ordering dynamics by observing that, if one considers just the transport of adsorbed CO coupled to the dynamics of surface relaxation, the restricted model that follows – consisting of eqns. (2.16) and (2.11) (without the kinetic source term) – belongs to the category of model C in the Hohenberg–Halperin classification.<sup>25</sup>

As mentioned before, the values of the rate constants for kinetic processes,  $k_{\text{CO}}$ ,  $k_{\text{O}_2}$ ,  $k_d$  and  $k_r$  are known from experiment with reasonable precision. In contrast, the thermodynamic parameters for the SPT –  $\Delta E$  and  $\alpha$  – have not been directly measured yet but they can be indirectly inferred from a scanning tunneling microscope (STM) study of the structural transformation,<sup>12</sup> in which the increasing number of nucleated  $1 \times 1$  patches was evaluated as a function of increasing CO exposure.

At a certain critical exposure, nucleation of small  $1 \times 1$  regions begins. This exposure value corresponds to a surface coverage of  $\theta_{\text{CO}} \approx 0.2$ . Apparently, the lifting of the reconstruction is completed at  $\theta_{\text{CO}} \approx 0.5$ .<sup>12,26</sup> Upon further CO exposure, the density of the  $1 \times 1$  phase increases monotonically, until eventually the saturation coverage,  $\theta_{\text{CO}} = 1$ , is attained. Assuming a simple proportionality relation between the number of patches and the surface state variable  $\kappa$ , and also between exposure and surface coverage ( $\theta_{\text{CO}}$ ), the experimental data can be fitted by the steady-state solution of eqn. (2.16):<sup>27</sup>

$$\kappa_s = \frac{1}{1 + \exp[(\Delta E - \alpha \theta)/RT]}. \quad (2.17)$$

In particular, the curve for  $\Delta E = 5.0/RT$ ,  $\alpha = 18.0/RT$ , drawn in Fig. 3 gives an excellent fit.

As usual, it is convenient to write the model equations in terms of adimensional variables and parameters.<sup>21</sup> Thus, upon substitution of (2.13) and (2.14) into respectively (2.11) and (2.12), we divide them both, as well as (2.16), by  $k_r$ . We now define a new adimensional time,  $\tau = k_r t$ , as well as the two adimensional pressures  $P_{\text{CO}} = p_{\text{CO}} k_{\text{CO}}/k_r$  and  $P_{\text{O}_2} = p_{\text{O}_2} k_{\text{O}_2} s_{\text{O}_2}/k_r$ .

We further note that the interfacial energy parameter appearing in (2.8) can be written as  $\gamma = RT \xi_0^2$ ,<sup>28</sup> where  $\xi_0$  is a phenomenological characteristic length related to the range of interactions. We then use this length to define a new adimensional space variable  $X = \xi_0^{-1} x$ . Upon these transformations, the model equations read:

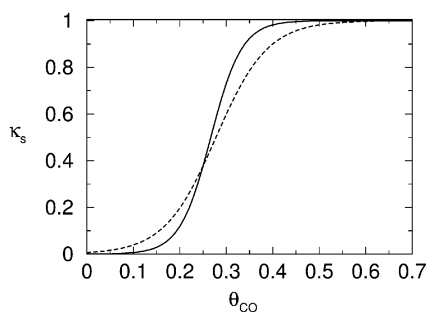


**Fig. 3**  $\kappa_s$  as a function of  $\theta_{\text{CO}}$  for  $\Delta E/RT = 5.0$ ,  $\alpha/RT = 18.0$  (dashed line). The sharper profile drawn as a solid line corresponds to a transition at room temperature ( $T = 300$  K), assuming that the dashed line is plotted at a temperature where spatio-temporal patterns are observed ( $T = 550$  K).

$$\frac{\partial \theta_{\text{CO}}}{\partial \tau} = P_{\text{CO}}(1 - \theta_{\text{CO}}^3) - d\theta_{\text{CO}} - \theta_{\text{CO}}\theta_{\text{O}} + \bar{M}\nabla^2 \left[ \ln \left( \frac{\theta_{\text{CO}}}{1 - \theta_{\text{CO}} - \theta_{\text{O}}} \right) - \bar{\alpha}\kappa - \nabla^2 \theta_{\text{CO}} \right] \quad (2.18)$$

$$\frac{\partial \theta_{\text{CO}}}{\partial \tau} = P_{\text{O}}(1 + \kappa)(1 - \theta_{\text{CO}} - \theta_{\text{O}})^2 - \theta_{\text{CO}}\theta_{\text{O}} \quad (2.19)$$

$$\frac{\partial \kappa}{\partial \tau} = -\bar{L} \left[ \Delta \bar{E} + \ln \left( \frac{\kappa}{1-\kappa} \right) - \bar{\alpha}\theta_{\text{CO}} \right], \quad (2.20)$$

where  $d = k_d/k_r$ ,  $\bar{M} = RTM/k_r \xi_0^2$ ,  $\bar{L} = RTL/k_r$ ,  $\bar{\alpha} = \alpha/RT$  and  $\Delta \bar{E} = \Delta E/RT$ . For the exponent characterizing precursor adsorption, that appears in eqn. (2.13), we took  $r = 3$ , the nearest integer smaller than the estimated value.<sup>14</sup>

In most situations, measuring quantities like the mobility is extremely hard.<sup>29</sup> Multiple competing effects concur to muddle the interpretation of results, particularly when surface reconstruction is involved.<sup>30</sup> Therefore, we will regard  $\bar{M}$  and  $\bar{L}$  as adjustable parameters. Choosing a value for  $\bar{L}$  did not prove hard because the period of homogeneous oscillations is quite sensitive to the choice of  $\bar{L}$ . This is easily understood because  $\bar{L}$  actually measures the speed at which the newly stabilized phase develops; and it is indeed the surface structure reversal, through the variation of the oxygen sticking probability, that is responsible for the oscillations, fixing their timescale. The value  $\bar{L} = 5.0 \times 10^{-4}$  yield a period of about 2 to 3 s, depending on the value of the other rate parameters, much the same as the typical time scale of the observed oscillations. We use it in all the simulations presented here.

### III. Numerical results in one dimension

We solved numerically eqns. (2.18)–(2.20) by a finite difference integration scheme at a fixed temperature – near 500 K corresponding to  $RT = 1$  (the energy parameters  $\Delta E$  and  $\alpha$  are in kcal mol<sup>-1</sup> and  $R$  in kcal mol<sup>-1</sup> K<sup>-1</sup>) – a value well inside the range where complex spatio-temporal phenomena was observed. In our study, we consider the reduced pressures  $P_{\text{CO}}$  and  $P_{\text{O}_2}$  as bifurcation parameters and proceed to an investigation of parameter space ( $P_{\text{CO}}-P_{\text{O}_2}$ ) in search for spatio-temporal behaviour of the kind observed experimentally.

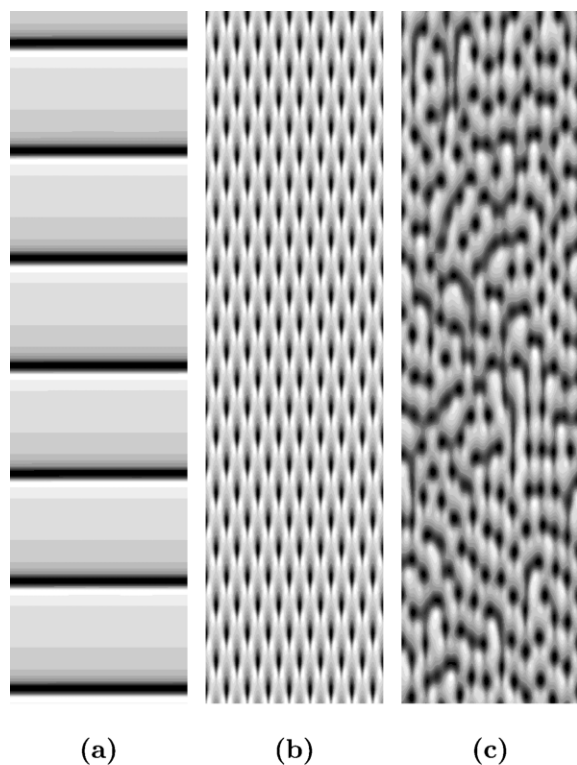
#### A. Spatio-temporal evolution

Fig. 4 shows space–time plots characteristic of the three types of spatio-temporal behaviour found in the simulations, respectively homogeneous oscillations (Fig. 4a), standing waves (Fig. 4b) and spatio-temporal chaos (Fig. 4c). To generate these plots, numerical integration of the model equations was performed in boxes made up of 256 discretization cells with no-flux boundary conditions (BC). The initial condition was, in every case depicted in Fig. 4, an uniformly distributed random noise with small amplitude, 500 to 1000 times smaller than the amplitude of oscillations. Time runs downwards and in each plot we show a segment of the evolution after about  $\tau = 200\,000$  – that is,  $4 \times 10^6$  integration steps – to lessen the chances that we were seeing transient behaviour.

We shall call the periodic solution with broken symmetry with respect both to time and space, shown in Fig. (4b), a standing wave although in rigour it is a standing-wave pattern superimposed on a homogeneous background oscillation. Indeed, after removing the contribution of the homogeneous mode by subtraction of the average

$$\bar{\theta}_{\text{CO}}(\tau) = \frac{1}{N_{\text{cel}}} \sum_{i=1}^{N_{\text{cel}}} \theta_{\text{CO}}^i(\tau), \quad (3.21)$$

where  $N_{\text{cel}}$  is the total number of integration cells, the pattern still does not meet all the symmetry requirements of a “true”



**Fig. 4** (a) Homogeneous oscillations:  $P_1 = 0.08277$ ,  $P_2 = 0.15$ ,  $\Delta E = 7.0$ ,  $\bar{\alpha} = 20.0$ ,  $d = 0.05$ , and  $\bar{M} = 0.0001$ . Spatial integration step:  $dx = 0.17$ ; time step:  $dt = 0.05$ .  $\theta_{CO}^{\min} \simeq 0.34$ ,  $\theta_{CO}^{\max} \simeq 0.64$ . (b) Standing waves:  $P_1 = 0.07532$ ,  $P_2 = 0.12$ ,  $\Delta E = 7.0$ ,  $\bar{\alpha} = 20.0$ ,  $d = 0.05$ , and  $\bar{M} = 0.0001$ ;  $dx = 0.17$ ,  $dt = 0.05$ .  $\theta_{CO}^{\min} \simeq 0.39$ ,  $\theta_{CO}^{\max} \simeq 0.59$ . (c) Spatio-temporal chaos:  $P_1 = 0.0735$ ,  $P_2 = 0.113$ ,  $\Delta E = 6.0$ ,  $\bar{\alpha} = 19.0$ ,  $d = 0.05$ , and  $\bar{M} = 0.0001$ ;  $dx = 0.12$ ,  $dt = 0.05$ .  $\theta_{CO}^{\min} \simeq 0.36$ ,  $\theta_{CO}^{\max} \simeq 0.57$ . No-flux boundary conditions (BC) on a 256 cell box. Time runs downwards. See text for further details.

standing wave. It does possess the discrete translational symmetries by one wavelength and one period  $x \rightarrow x + 2\pi/q$ ,  $t \rightarrow t + 2\pi/\omega$ , where  $q$  is the wave-vector and  $\omega$  the frequency, but the combined symmetry of time translation through a half period ( $t \rightarrow t + \pi/\omega$ ) and inversion  $u(x) \rightarrow -u(x)$ , with  $u(x) = \theta(x) - \bar{\theta}$ , is not verified. On the other hand, the pattern remains unchanged by a simultaneous time shift by half a period and translation by half wavelength  $t \rightarrow t + \pi/\omega$ ,  $x \rightarrow x + \pi/q$ , making it a *sub-harmonic* pattern with a general analytic expression

$$u(x) = A_H e^{2i\omega t} + A_L e^{i(\omega t + qx)} + A_R e^{i(\omega t - qx)} + \text{c.c.} \quad (3.22)$$

where the subscripts H, L and R stand for the homogeneous mode, left- and right-going waves, respectively.

Furthermore, there are no “real” nodes where the amplitude of the local oscillations actually vanishes, although between the sharp depressions which build up in alternate movements every half period, there are a few points that oscillate with very small amplitudes.

In terms of the underlying physics, the resonant pattern can be interpreted as resulting from periodic nucleation and growth of phase separated domains. As the system is periodically driven inside and out the thermodynamically unstable region, there is an outbreak of phase separated domains which subsequently synchronizes by the coupling effect of the homogeneous mode. Much like phase separation may become “frozen” in the presence of chemical reactions,<sup>31</sup> here full phase separation is not accomplished because domain coarsening is alternately promoted and inhibited by the effect of the global oscillation.

Only in a limited interval of values of  $\theta_{CO}$  and  $\kappa$  can phase separation take place. If during one period of oscillation, the system’s variables only assume those values for a short while, phase separated domains will not have enough time to develop and the system will be kept spatially uniform. This is what happens in the case of the relaxation oscillations of Fig. 4a. Under those conditions, the system spends most of the time outside the two-phase region and only a very short period going across the unstable domain. It is an insufficient period of time to allow density fluctuations to grow to macroscopic size and thus a stable structured pattern can never emerge. As the oscillation profiles get smoother, the part of the cycle spent inside the unstable region increases and may become comparable to the characteristic time of phase separation, ultimately leading to a resonant spatio-temporal pattern. This explains why relaxation oscillations with large periods (and stiff profiles) are uniform while standing wave patterns usually appear associated with fast, smoother oscillations.

The above picture is consistent with theory and observations of periodic spinodal decomposition,<sup>32</sup> where a system is forced periodically into the unstable region of the thermodynamic phase diagram. Periodic spinodal decomposition is realized by cyclic variation of the reduced temperature  $T/T_c$ , either by means of direct temperature forcing or by imposing a pressure modulation (which changes  $T_c$ ). Theory predicts that an important parameter is, in fact, the ratio of the period of the quench to the time scale of domain growth dynamics.<sup>32</sup> If this ratio is  $\ll 1$ , the period of the quench is much too short to produce any significant effects. On the other hand, if the ratio is too large, then phase separation proceeds without limit. Between the two limiting cases, there is periodic enhancement and destruction of (large) density fluctuations, which may lead to self-sustained patterns.

A strong numerical evidence supporting the above interpretation is provided by the transient regime that precedes the establishment of a spatio-temporal pattern.<sup>27</sup> Total synchronization of the surface happens fast, and in a couple of periods at most no trace is left from the uniformly distributed random noise imposed as initial condition. A spatial modulation develops then, the amplitude of which shrinks when the homogeneous carrier oscillation approaches its extrema, while growing down the slope of the oscillation profile in a kind of breathing motion. The maximum amplitude of the spatial modulation grows steadily, period after period, yet the whole pattern continues to oscillate in phase. At some point the amplitude of the modulation is large enough to cause a resonance with the homogeneous mode. Suddenly, the phase coherence of the ensemble of strongly coupled oscillators is broken as neighbouring minima start to oscillate out of phase. Finally a standing wave with twice the wavelength of the initial modulation is stabilized.

The period of the pattern, that is the time it takes for a structure to reproduce itself exactly, is doubled with respect to the period of the averaged field. We are thus in presence of a 2 : 1 resonance with each cell oscillating at half the frequency of the average. This feature is evident from Fig. 5, where in the upper and middle boxes we plot the time evolution of two cells arbitrarily chosen among the 256 integration cells while the evolution of the mean coverage  $\bar{\theta}_{CO}$ , given by (3.21), is represented in the lower box.

It is significant that we have always found a strong wave-number selection in this system. In the simulations we were able to produce stable standing waves of up to twelve wavelengths by increasing the system size. Further numerical tests showed that the wavelength was clearly intrinsic, depending only on the external parameters (temperature, pressures, *etc.*) and the mobility  $M$  (which itself must depend on  $T$ ). Certainly it does not change with the boundary conditions, apart from the obvious restriction imposed by periodic boundary conditions, that is, that only an integer number of wavelengths

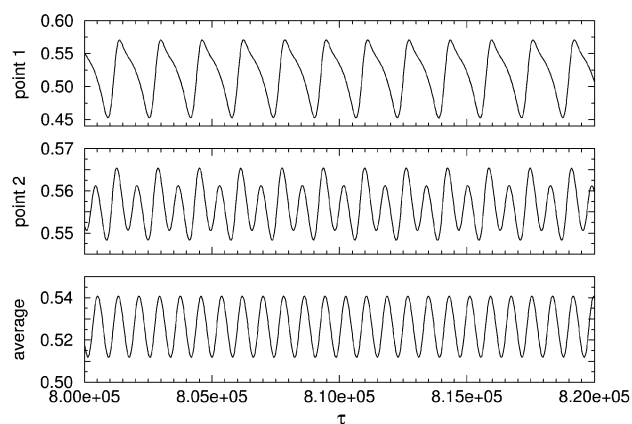


**Fig. 5** Temporal evolution of the CO coverage at two given points on the spatial grid compared with the evolution of the average  $\theta_{\text{CO}}$  (lower box). Parameters are the same as in Fig. 4(b).

can be present. Notwithstanding, with no-flux boundary conditions we found a tendency for structures with half integer number of wavelengths to be stabilized, particularly in smaller systems.

## B. Existence diagram

Fig. 6 shows the existence diagram of the four classes of spatio-temporal behaviour found in the simulations – namely homogeneous oscillations, standing waves, turbulence and stationary patterns. With this set of fixed energetic and kinetic parameters (see caption), all those kinds of patterns may be obtained simply by varying the reactants partial pressures. We believe that the ability of the model to reproduce this scenario is of great significance because in the experiments, the CO and O<sub>2</sub> partial pressures are the only externally tunable parameters. Indeed, the remaining parameters being related to the properties of the substrate and reactant species as well as to the temperature, they are not allowed to change during one particular experiment conducted under isothermal conditions. But transitions between the three different types of spa-

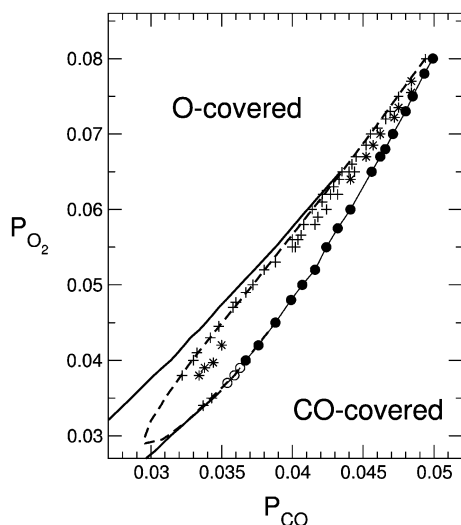


**Fig. 6** The domain of complex spatio-temporal behaviour in 1D. Parameters are  $\Delta E = 5.0$ ,  $\bar{\alpha} = 18.0$ ,  $d = 0.03$ ,  $\bar{M} = 5.0 \times 10^{-5}$ , and  $\bar{L} = 5.0 \times 10^{-4}$ . The filled circles represent uniform relaxation-type oscillations with very long periods. The crosses (+) are standing-wave solutions (all of them 2 : 1 resonances) and the stars (\*), turbulent patterns. Finally the solid lines connect points where the Turing bifurcation takes place.

tio-temporal patterns were observed under precisely the above conditions, just by varying  $p_{\text{CO}}$  and  $p_{\text{O}_2}$ .<sup>2</sup>

Transitions from steady-state to oscillatory behaviour occur discontinuously at the high  $P_{\text{CO}}$  side, for values of the oxygen partial pressure above  $P_{\text{O}_2} \approx 0.04$ . Following a decrease in the CO partial pressure, the oscillatory region is accessed through a saddle-node infinite period bifurcation (SNIPER) leading to relaxation-type homogeneous oscillations (filled circles). The behaviour close to the bifurcation point  $P_{\text{CO}}^c$  is not altered by the action of the spatial terms as demonstrated by the fact that the oscillation period diverges as  $T \sim 1/\sqrt{\delta}$  as  $\delta \rightarrow 0$ ,<sup>27</sup> where  $\delta$  measures the distance from the bifurcation point:  $\delta = |P_{\text{CO}} - P_{\text{CO}}^c|$ .

The domain of oscillatory behaviour in the absence of transport terms is also represented in Fig. 6. Setting  $\bar{M}$  to zero in eqn. (2.18) and integrating the resulting set of ODEs, one finds oscillations inside a region which has the shape of an airfoil. The oscillatory region is bounded from the left by a (dashed) line of Hopf bifurcations which starts right at the cusp, reaches a turning point in the lower part of the diagram – approximately at  $P_{\text{CO}} \approx 0.0295$ ,  $P_{\text{O}_2} \approx 0.291$  – and rises again to meet the line of SNIPER bifurcations, thereby closing the oscillatory domain. To the right of the oscillatory region, the system assumes homogeneous steady states of high CO coverage while to the left the surface is also uniformly covered but now with a higher percentage of oxygen. Crossing the oscillatory region causes a discontinuous transition between these states, labeled in the existence diagram of Fig. 6 as “CO-covered” and “O-covered” respectively. However, this is not meant to imply that the surface is fully covered with either CO or oxygen. Indeed, in the range of partial pressures where oscillations occur  $\theta_{\text{O}}$  is always small, below 0.2. The CO coverage, on the other hand, assumes high values immediately to the right of the SNIPER line, where the surface is close to saturation because there the corresponding value of  $\kappa$  is almost one (see Fig. 3).

The pure kinetic model (*i.e.* without diffusion) has an oscillatory domain which is very similar in shape and structure to that of the KEE model, for which a comprehensive bifurcation analysis has been performed.<sup>14,33</sup> This comes as no surprise because, when diffusion is neglected, the present model and its predecessor differ only in their respective descriptions of surface relaxation (eqn. (2.20)). On the other hand, the shape of the oscillatory region is controlled mainly by the bistable properties of the reaction terms<sup>14</sup> – that is eqns. (2.18)–(2.19) – which practically do not change with respect to the KEE model.

As one keeps on decreasing  $P_{\text{CO}}$  beyond the SNIPER line, the period of homogeneous oscillations drops fast and these assume less stiff profiles while remaining spatially uniform. Then transitions either to standing waves or spatio-temporal chaos take place. Wide hysteresis loops associated with these transitions make it impossible to draw definite boundary lines separating the three classes of solutions, much less represent them with clarity. Therefore in Fig. 6, only those points connected by a line correspond to bifurcating solutions, obtained following an adiabatic variation of the control parameter,  $P_{\text{CO}}$ , along a horizontal path of constant  $P_{\text{O}_2}$ . On the other hand, the crosses (+) and stars (\*) represent solutions obtained by pressure quenches into the oscillatory domain, respectively standing-waves and spatio-temporal chaos. In every case the initial condition is the closest homogeneous steady-state solution perturbed with a uniformly distributed random noise of small amplitude.

In a small section of the boundary line – in the range  $0.036 \lesssim P_{\text{O}_2} \lesssim 0.04$  – the instability of the homogeneous steady state generates immediately standing waves. These points are represented by empty circles in Fig. 6. They lie close to the point where the set of ODEs displays a codimensional-two bifurcation (Hopf–SNIPER) point. The influence of the SNI-



PER bifurcation is apparent from the fact that the oscillations on the average  $\bar{\theta}_{\text{CO}}$ , at twice the frequency of a given point, retain their relaxational character.

By increasing  $P_{\text{CO}}$  the instability region can be entered from the left side. In this case two situations may occur. Provided  $P_{\text{O}_2}$  is high enough, the first bifurcation is a soft mode Hopf bifurcation leading to small amplitude homogeneous oscillations. Their amplitude grows steadily as the distance from the threshold increases until beyond a second threshold, the uniform oscillations become unstable leading to a standing wave pattern whose period is twice that of the original uniform oscillations.

A different (and complementary) scenario is observed at lower  $P_{\text{O}_2}$  values. There, once the bifurcation line is crossed, the oscillations present a smooth spatial modulation. In this case, the period of the spatio-temporal structure is the same as that of the homogeneous mode. The resulting space-time plot, represented in Fig. 7a, reveals a 1 : 1 resonance. This solution is only stable in a narrow parameter range, being replaced by the 2 : 1 subharmonic pattern of Fig. 7b upon a further (small) increase in the bifurcation parameter,  $P_{\text{CO}}$ .

A third scenario for the onset of standing waves is found in the lowermost part of the diagram when entering the instability region by either side. In both cases one encounters first a bifurcation breaking the symmetry in space only. The amplitude of these steady-state structures grows with increasing distance from each threshold, and when this distance is further increased, a standing-wave pattern develops whose spatial period is doubled with respect to the stationary structure. If the variation of the control parameter proceeds in really small steps (adiabatically), a 1 : 1 resonance is stabilized in between, though again it only remains stable through a very narrow parameter range. This mixed-mode state, typical of the interaction between a Turing and Hopf bifurcation,<sup>34</sup> is identical to that shown in Fig. 7a. Also, the 2 : 1 resonant patterns are qualitatively indistinguishable whether they emerge following the instability of the homogeneous Hopf mode, through a spatial subharmonic instability, or bifurcate from the 1 : 1 spatio-temporal structure.

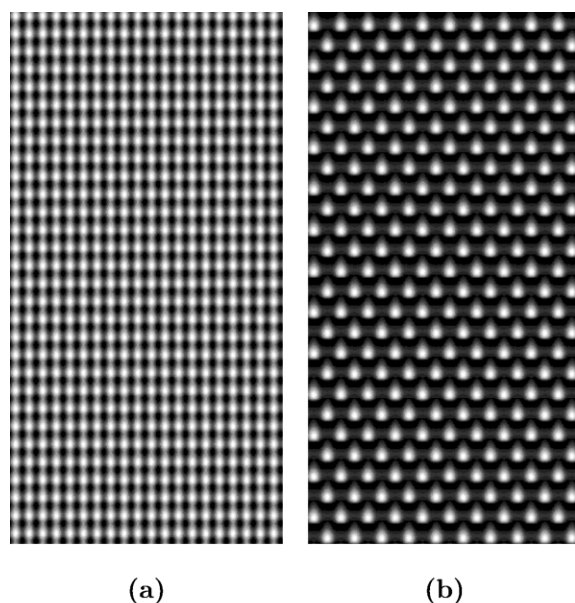


**Fig. 7** Spatio-temporal charts showing 1 : 1 and 2 : 1 resonances as the control parameter  $P_{\text{CO}}$  is varied at fixed  $P_{\text{O}_2} = 0.06$ ,  $\Delta E = 5.0$ ,  $\bar{\alpha} = 18.0$ ,  $d = 0.03$ ,  $\bar{M} = 0.00005$ ,  $dx = 0.08$  and  $dt = 0.05$ . (a) a 1 : 1 resonance at  $P_{\text{CO}} = 0.0413$ :  $\theta_{\text{CO}}^{\text{min}} \approx 0.19$ ,  $\theta_{\text{CO}}^{\text{max}} \approx 0.36$ . (b) 2 : 1 pattern at  $P_{\text{CO}} = 0.04135$ :  $\theta_{\text{CO}}^{\text{min}} \approx 0.17$ ,  $\theta_{\text{CO}}^{\text{max}} \approx 0.576$ . The integration time,  $\tau = 20\,000$ , number of cells (256) and BC (periodic) are the same for both charts. Time runs downwards.

On the transition to spatio-temporal chaos, the standing wave pattern undergoes a modulational instability which, upon further increase of the control parameter, leads to a state characterized by the proliferation of spatio-temporal defects. On the approach to the SNIPER line, moving away from the Hopf bifurcation line through an increase in  $P_{\text{CO}}$ , the transition to turbulent patterns probably occurs by a generic mechanism proposed recently by Argentina *et al.*,<sup>35</sup> the fundamental idea being that a spatially homogeneous, though anharmonic, limit cycle may act as a parametric forcing on itself. Using a very simple model, they have shown that such limit cycle is generically unstable with respect to inhomogeneous perturbations on the approach to a homoclinic bifurcation. The instability leading to spatio-temporal chaos is either period-doubling, with a finite wavenumber, or a phase instability. This behaviour, which we have termed self-resonance and they call self-parametric forcing, is more likely to take place near the apex of the bifurcation diagram because it is there that the homoclinic limit cycle closes on the Hopf bifurcation.

The model also predicts stationary structures (Turing patterns) in a strip that is the continuation of the oscillatory region to lower partial pressures. This region, of which only a small part is shown in Fig. 6, is even larger than the oscillatory domain. Although the predicted structures are characterized by small amplitudes – with spatial variations in oxygen coverage smaller than 0.1 and in  $\theta_{\text{CO}}$  of less than 0.3 – it should be possible to observe them by the imaging techniques used to monitor spatio-temporal patterns, including PEEM (see below). The formation of Turing patterns in the CO oxidation on Pt(110) has been suggested (namely in ref. 2) but never clearly established experimentally. We hope that forthcoming experimental work will address this important issue.

## VI. Spatio-temporal patterns on the catalytic surface

The majority of experimental images of the Pt(110) surface showing spatio-temporal patterns during CO oxidation were obtained with the photoemission electron microscope (PEEM). The presence of adsorbate molecules alters the work function of the substrate to a different measure depending on the adsorbed species and the particular surface phase on which adsorption is taking place. The PEEM essentially probes the *local* values assumed by the work function, with a typical spatial resolution of  $\sim 1\,\mu\text{m}$ . By significantly increasing the work function, the presence of adsorbed oxygen reduces the photoemission of electrons, while in regions predominantly covered by CO, the electron yield is only weakly decreased. Therefore, regions where oxygen coverage is high appear dark in the PEEM images, whereas those covered mostly by CO are bright. The PEEM is very sensitive to variations in oxygen coverage: it is expected to detect variations in  $\theta_{\text{O}}$  as low as 0.5%.

In the presentation of two-dimensional results that follows we shall adopt the same convention. Snapshots of the oxygen coverage field,  $\theta_{\text{O}}(r)$ , are displayed in a 256 step grey scale, where white corresponds to minimum oxygen coverage and black to the maximum value of  $\theta_{\text{O}}(r)$ . Since  $\theta_{\text{CO}}(r)$  and  $\theta_{\text{O}}(r)$  are strictly anti-correlated in time, the CO coverage field at a given instant is practically the negative image of the oxygen coverage pattern at the same moment. The pattern of reconstructed and unreconstructed regions, *i.e.* the spatial modulation of the variable  $\kappa$ , strictly follows the distribution of CO on the surface and therefore the reconstruction patterns are out of phase of  $\pi$  with the oxygen coverage patterns. Note that a linear relation between brightness and coverage is implicit, although some observations suggest that it may be non-linear<sup>36</sup> or that, being (piecewise) linear, show crossover behaviour between two different slopes from low to moderate oxygen coverages.<sup>30</sup>

### A. Subharmonic standing-wave patterns: oscillating squares and rhombs

We performed extensive numerical simulations of the model equations (2.18)–(2.20) in two dimensions. These have revealed the same four classes of spatio-temporal dynamics found in the one-dimensional simulations, namely homogeneous relaxation-type oscillations, standing wave patterns, chemical turbulence as well as stationary structures. There is no substantial difference in the nature of spatially uniform periodic solutions with respect to the one-dimensional case; the whole surface simply oscillates monotonously in phase. As in 1D, homogeneous oscillations can be found mainly near the SNIPER boundary, that is on the high  $P_{\text{CO}}$  side and at moderate to high values of  $P_{\text{O}_2}$  (relatively to the existence range of oscillations). What must be stressed here is that, when the dynamics of the SPT is considered, spatial coupling alone is sufficiently strong to allow homogeneous oscillations to occur in 2D with all cells oscillating with the same frequency and in phase.

The frame sequence displayed in Fig. 8 shows a subharmonic standing-wave pattern with square symmetry. To avoid redundancy, we have only represented there the evolution during half a period. Notice that in the last frame the points where the oxygen coverage is lower – the bright regions – are displaced by one-half wavelength in the vertical and horizontal directions with respect to the first frame. The second half-period merely repeats the sequence shown in Fig. 8 only at shifted locations as mentioned before, until the pattern in the first frame is recovered.

On the other hand, we can distinguish in Fig. 8 a slow modulation of the oscillation amplitude reflected in a smooth undulation in the brightness of the patterns. This effect is also seen in experimental videos.<sup>2,3</sup> In the simulations, when the standing-wave structure first emerges from homogeneous oscillations it is perfectly phase coherent and remains so for a long time, up to several dozens or even hundreds of periods. But even in the most stable cases it is likely that as time progresses an amplitude modulation will eventually develop. In the case of Fig. 8 the magnitude of the modulation has already saturated.

Up to this point we have considered an isotropic system. However, as can be seen in the ball model of Fig. 1, the Pt(110) surface is markedly anisotropic either in its reconstructed missing-row form as well as in the bulk-like termination state. Thus, CO diffusion is expected to proceed considerably faster along the troughs in the  $[1\bar{1}0]$  direction

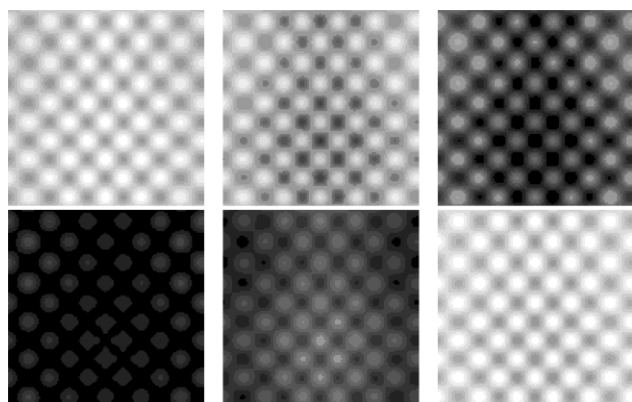


**Fig. 8** Evolution of a square standing-wave pattern during half a period. Parameter values are  $P_{\text{CO}} = 0.0728$ ,  $P_{\text{O}_2} = 0.11$ ,  $\Delta E = 5.0$ ,  $\bar{\alpha} = 18.0$ ,  $d = 0.05$ , and  $\bar{M} = 5.0 \times 10^{-5}$ . From left to right, top to bottom, the time between two consecutive images is respectively  $\tau = 200$ , 120, 100, 140, and 220. Periodic BC. The grey scale was calibrated over one oscillation period, so that white corresponds to the absolute minimum and black to the absolute maximum assumed by the variable  $\theta_{\text{O}}$  among the  $128 \times 128$  cells.

than in the perpendicular, “cross-row”  $[001]$  direction. Moreover, in view of the larger channels of the reconstructed surface, one should expect faster diffusion along the  $[1\bar{1}0]$  direction on the  $1 \times 2$  than on the  $1 \times 1$  phase. As mentioned before, CO diffusion measurements are extremely hard to perform and the results have a difficult interpretation because of the CO-induced lifting of the reconstruction. On the other hand, only for low temperatures ( $T < 300$  K), does the phase transition proceed sufficiently slow for diffusion to occur on either surface structure. In that range, experiments have reported a difference between the diffusion coefficients of CO on the two surface structures,<sup>30</sup> with diffusion on the  $1 \times 1$  surface being slower. However, these findings cannot be straightforwardly extrapolated to the temperatures at which spatio-temporal patterns are observed because there the CO-induced SPT is fast enough so that both processes interfere.

In spite of these and other shortcomings that confound the interpretation of experimental results, the anisotropy of CO diffusion on both surface phases has been clearly established.<sup>30,36</sup> Here we shall consider diffusion anisotropy in the most straightforward way: we simply put  $\bar{M}_y = \rho \bar{M}_x$ , where  $\bar{M}_x$  and  $\bar{M}_y$  are the (reduced) mobilities of adsorbed CO in the  $x$  and  $y$  direction respectively. This means we are neglecting the structural dependence of anisotropic transport in the adlayer. To maintain consistency we also scale the phenomenological characteristic length as  $\xi_{0y} = \sqrt{\rho} \xi_{0x}$ . Using a value of  $\rho > 1$  we were able to reproduce a standing-wave structure where the maxima and minima of oxygen coverage form a pattern with a symmetry of rhombs. The evolution of such a pattern, with  $\rho = 4$ , is shown in Fig. 9. Like in the experimental images, the rhomb’s longer axis is in the  $[1\bar{1}0]$  direction – the vertical ( $y$ ) direction in the simulations.

The simulations (Fig. 9) reveal regular rhomb-shaped patterns that do not present any topological defects, such as dislocations and disclinations. In contrast, the experimentally observed patterns appear distorted,<sup>2</sup> maybe due to the presence of surface defects – perhaps terrace ledges – which would introduce an element of disorder in an otherwise well organized structure. These microscopic effects are outside the scope of our model which so far describes only a perfect surface. On the other hand, the experimental images of rhomb-shaped standing waves display a markedly higher contrast with well defined oxygen “droplets” emerging from a predominantly CO-covered background (bright).<sup>2</sup> As we see in Figs. 8 and 9, the model equations yield rather standing-wave patterns which are smooth modulations of the coverage fields  $\theta_{\text{O}}$  and  $\theta_{\text{CO}}$ , and do not display sharp boundaries between domains of each adsorbed species. In this vein, the standing-wave patterns of Figs. 8 and 9 are representative of that particular regime which in the context of phase ordering dynamics is called the weak segregation regime. The terminology is appropriate because, as stressed before, it is indeed the surface phase transition that is behind the segregation of the adsorbate species on the surface and furthermore, analogous time-independent structures appear in frozen phase separation.<sup>31</sup> In an identical sense, the experimental patterns are then examples of strong segregation. In 1D simulations we were able to repro-

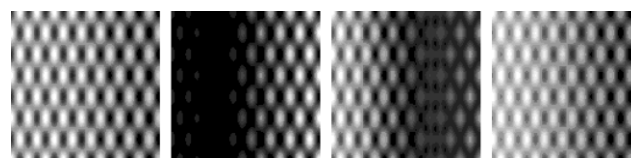


**Fig. 9** Evolution of a standing-wave pattern with a symmetry of rhombs. Parameter values are  $P_{\text{CO}} = 0.0811$ ,  $P_{\text{O}_2} = 0.14$ ,  $\Delta E = 5.0$ ,  $\bar{\alpha} = 18.0$ ,  $d = 0.05$ , and  $\bar{M} = 5.0 \times 10^{-5}$ . Time lag between consecutive images is  $\tau = 300$ , 50 and 250 respectively. A strong long-wavelength modulation is apparent.



duce both the weak and the strong segregation regimes by varying the value of  $d$ . Lower  $d$  corresponds to lower CO desorption – thus lower  $T$  – and results in more stiff *spatial* profiles. (Compare Figs. 4b and 7b and remark that the latter is “painted” in black and white while the former displays gradual changes between shades of grey.) However, in two-dimensions we could not do the same without provoking a symmetry modification, as we discuss below.

### B. Subharmonic standing-wave patterns: stripes

In our simulations, standing-wave patterns with sharp interfaces occur when CO desorption takes place at a lower rate. The image sequence of Fig. 10 was obtained at  $d = 0.03$  (the same value we used to put together the existence diagram in Fig. 6). The energetic parameters are those leading to squares (rhombs) in Fig. 8 (9). Altering these parameters – which must be changed in synchrony so that oscillations persist – had only little impact on the symmetry of the solutions; stripe patterns are quite robust with respect to these changes. The value of  $d$ , on the other hand, proved determinant for the onset of one or the other structure. Moreover, when  $d$  is lowered,  $\bar{M}$  has to be decreased also in order that spatio-temporal patterns are still obtained. This reinforces the idea that oscillating stripes should be the asymptotic solution at lower temperatures. The stripes were perfectly regular and no low frequency modulation similar to that encountered in the case of rhombs was observed. This contrasts with experimental stripes that display irregularities in the form of undulations and dynamic displacements.<sup>3</sup>

A feature which compares well to experiment<sup>3,18</sup> is the fact that the beginning of an half-cycle is marked by the emergence of a dark O-rich front that splits the CO-covered band in two creating a pair of stripes which move apart. These stripes then collide and merge one wavelength away, only to be separated again later by a new splitting front growing from within, so that the initial pattern is repeated. During a small part of the half-cycle, a thin strip of oxygen is still visible in the middle of the areas of high CO coverage – particularly in the fourth frame in the sequence of Fig. 10. The reciprocal case, where a bright CO front bursts from the middle of a dark O-rich band was also observed but now in the high  $P_{O_2}$  region of the existence diagram (see Fig. 6), namely at  $P_{CO} = 0.0385$ ,  $P_{O_2} = 0.052$ . This indicates that the splitting front is that of the minority phase.

Note that Fig. 10 represents the evolution of an isotropic system, which clearly shows that the stripe pattern (like the square pattern before) is indeed a broken symmetry solution of the original set of pdes (eqns. (2.18)–(2.20)) and not in

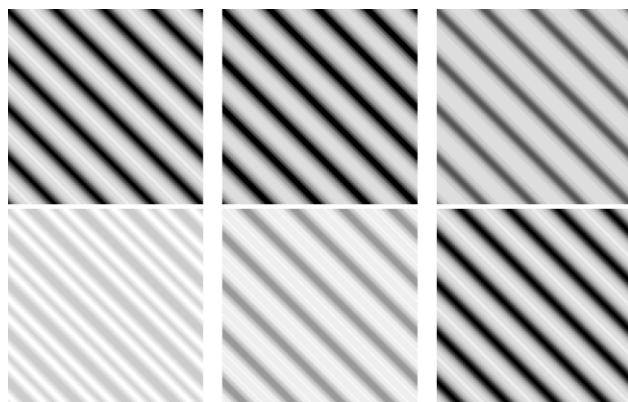


**Fig. 10** Evolution during half a period of a standing-wave pattern with stripe symmetry. Parameter values are  $P_{CO} = 0.0353$ ,  $P_{O_2} = 0.037$ ,  $\Delta E = 5.0$ ,  $\bar{\alpha} = 18.0$ ,  $d = 0.03$ , and  $\bar{M} = 2.5 \times 10^{-5}$ . From left to right, top to bottom, the time lag between two consecutive images is respectively  $\tau = 100, 200, 200, 300$  and  $400$ . Periodic BC.

any way the result of anisotropic transport. If we introduce surface anisotropy in the rather simple way we did in the last section, the stripes tend to line up with the direction of fast transport. However, even an unrealistically high value of the anisotropy parameter  $\rho$  is insufficient to align stripes along the  $[1\bar{1}0]$  direction. We are therefore led to the conclusion that a more sophisticated treatment of surface anisotropy is necessary, not only to explain this particular experimental fact, but to access the full implications of anisotropic effects on the symmetry of patterns.

### C. Turbulent patterns

Images of turbulent spatio-temporal patterns obtained in simulations are shown in Fig. 11, where we see stripe fragments with poor spatio-temporal coherence among small irregular patches. The two snapshots were taken at an interval of  $\Delta\tau = 720$ , which in the temperature range in which turbulent behaviour has been reported<sup>2</sup> ( $T \approx 540$  K) corresponds to about 2 s. Note that during that short period of time the structure has evolved considerably, with large regions that were predominantly bright in the first image appearing dark in the second. The short time scale associated with the turbulent regime in the simulations matches the observed characteristic time of evolution. In spite of the broad similarities, a closer inspection of the simulated patterns shows that they are more structured than experimental ones.

Associated with turbulent patterns are oscillations on the local surface coverage which are highly irregular and of large amplitude. Oscillations in the averaged coverages and in the average ratio of the  $1 \times 1$  phase,  $\kappa$ , are also chaotic but with a much smaller amplitude, which at its highest value is only about 10% of the maximum amplitude of the local oscillations.

### D. Target patterns

At lower temperatures, around 430 K, simultaneously with oscillations in the reaction rate, the surface exhibits target patterns, that is concentric waves emanating periodically from a nucleation centre.<sup>2,3,37–39</sup> The wave fronts are elliptically shaped, with the longer axis along the  $[1\bar{1}0]$  direction, while the shorter axis coincides with the  $[001]$  orientation of the Pt(110) surface. The regions between the concentric waves switch periodically from dark to bright. Likewise, the brightness of the fronts is also reversed but in opposite sense with respect to the bulk. Each time the surface undergoes a bulk oscillation, the outermost wave of the targets is annihilated. Nevertheless, the target as a whole still grows, since the subsequent waves arise beyond the zone where the last annihilation took place. The switching of the background intensity over the entire surface area occurs quite rapidly, in less than one fifth of the global oscillation period, approximatively. This fea-

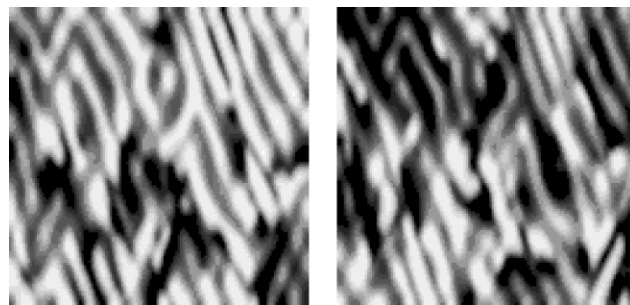


**Fig. 11** Simulated turbulent patterns at  $P_{CO} = 0.047$ ,  $P_{O_2} = 0.072$ ,  $\Delta E = 5.0$ ,  $\bar{\alpha} = 18.0$ ,  $d = 0.03$ , and  $\bar{M} = 2.5 \times 10^{-5}$ . The two snapshots were taken after a transient of  $\tau = 250\,000$ . The value of the anisotropy parameter is  $\rho = 4$  and the interval between the two images is  $\Delta\tau = 720$ ;  $\theta_O^{\min} \approx 0.01$ ,  $\theta_O^{\max} \approx 0.28$ .

ture is consistent with the relaxation-type oscillations observed in the integral reaction rate.

As in most oscillating chemical systems displaying target patterns, the precise nature of the pacemaking centres is still unclear. However, it is commonly accepted that these are due to some kind of surface imperfection, an assertion supported by observations that the target patterns will reappear at the same spots when the experiments are repeated. Most likely, the nucleation region from where the wave fronts periodically emanate consists of patches of enhanced step density or enhanced concentration of impurity atoms, but the possibility that some other type of surface imperfection may trigger surface waves cannot be excluded.

Nucleation of reaction fronts at defects is a complex dynamical process, the details of which are not yet understood. For example, both the geometrical form of the defect as well as its inner heterogeneities can be decisive factors in the nucleation process.<sup>39</sup> The mean field approach is, of course, unsuited to deal with these microscopic details. Thus, we shall look upon target formation on a coarser spatial scale, considering the pacemaking centres as regions of higher concentration of defects, on the average.

The best guess as to the role of surface defects in this process is that they lead to a noticeable increase in the local oxygen sticking coefficient and hence to improved reactivity. Oxygen adsorbs preferentially along step edges,<sup>13</sup> a fact that is behind the higher oxygen sticking coefficient observed in the channelled  $1 \times 2$  surface, as mentioned before. Presumably, this is due to the fact that oxygen adsorption is dissociative. In this vein, defects should not affect CO adsorption, matching existing data which show no noticeable variation in the CO sticking coefficient between the  $1 \times 1$  and  $1 \times 2$  surfaces.

To the above hypothesis we have added the assumption that the oxygen sticking coefficient is increased in the same proportion irrespectively of the state of the surface, that is as much in the  $1 \times 1$  as in the  $1 \times 2$  phase. This is a strong assumption, most certainly not verified when the majority of defects present are dislocations or vacancies which may relax together with surface structure. Notwithstanding, it is expected to be valid when the defect region consists rather of patches of enhanced step density or higher concentration of impurity atoms. With the former assumption, an increase in the local oxygen sticking coefficient is strictly equivalent to an increase in the local value of the adimensional pressure  $P_{O_2}$ . Thus we set in the defect region

$$P_{O_2}^{\text{def}} = P_{O_2}(1 + \sigma), \quad (4.23)$$

where  $P_{O_2}$  is the reduced oxygen pressure elsewhere on the surface and  $\sigma$  is a positive parameter measuring the increase in sticking probability ( $\sigma = 0$  corresponds to the defect-free situation).

In the parameter range of our simulations, target patterns exist only in a small domain of the reactants partial pressures. On every occasion we found a threshold for  $\sigma$  below which no waves are produced in agreement with prevailing theories,<sup>40</sup> but this threshold value was always small. The ellipticity of the patterns follows directly from our uninvolved approach to surface anisotropy; the anisotropy ratio  $\rho$  was chosen so that the aspect ratio of the simulated patterns approximatively matches the observed eccentricity.

It must be noted that in our simulations target patterns were found mainly associated with quasi-harmonic oscillation profiles while experimentally observed targets consist of trigger waves associated with relaxation-type oscillations in the integral reaction rate. But, exceptionally, we have also found targets made up of propagating wave fronts with sharp boundaries like the one shown in Fig. 12a, associated with stiff oscillation profiles displayed by the reaction rate in the bulk. The switching of the background intensity is then considerably

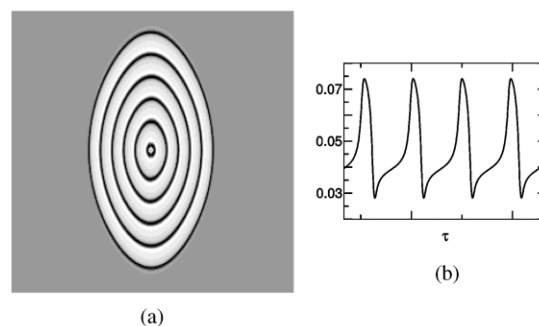


**Fig. 12** (a) Target pattern consisting of sharply defined wave fronts. (b) Relaxation-type oscillation in the rate of  $\text{CO}_2$  production associated with the pattern on the left. Parameter values are the following:  $P_{\text{CO}} = 0.09282$ ,  $P_{\text{O}_2} = 0.2$ ,  $\Delta E = 8.0$ ,  $\bar{\alpha} = 21.0$ ,  $d = 0.05$ ,  $\bar{M} = 5.0 \times 10^{-5}$ ,  $\sigma = 0.05$ ,  $\rho = 4.0$ ,  $dx = 0.5$ , and  $dt = 0.2$ .  $\theta_{\text{O}}^{\text{min}} \simeq 0.04$ ,  $\theta_{\text{O}}^{\text{max}} \simeq 0.23$ .

fast (Fig. 12b). Target patterns which look remarkably similar to that of Fig. 12a were reported in ref. 37.

### E. Spiral waves in an oscillatory background

In addition to target patterns, experiments revealed spiral waves in a large temperature range<sup>2,3,37,39,41</sup> both under oscillatory as well as excitable conditions. Like target patterns, the observed spirals are elliptically deformed. Unlike the former, for fixed external parameters the spirals exhibited a continuous distribution of wavelengths and periods. This is understood by the fact that most spirals are pinned to surface defects of markedly distinct shapes and sizes. Frequently one observes a number of freely rotating, meandering spirals<sup>39,41</sup> but most of the spirals in this system have their cores fixed to structural defects.

Notwithstanding, for the formation of spirals no heterogeneity at the centre is needed; only a certain topological condition must be satisfied by the initial concentration distribution, as offered, most simply, by the broken end of a wave front.<sup>40</sup> With such an initial condition we obtained the pattern shown in Fig. 13. Under the same set of parameters, if the initial condition was completely random, the system would exhibit homogeneous relaxation-type oscillations. Just like it happened with target wave fronts, the spiral arms alternate in brightness always in opposition to the bulk and the front mimics the profile displayed by uniform oscillations in the absence of the defect. Note that both the revolution period and the wavelength are intrinsic properties; they depend not



**Fig. 13** Elliptic spiral wave on an oscillating background. The parameter values are  $P_{\text{CO}} = 0.0775$ ,  $P_{\text{O}_2} = 0.13$ ,  $\Delta E = 7.0$ ,  $\bar{\alpha} = 20.0$ ,  $d = 0.05$ ,  $\bar{M} = 5.0 \times 10^{-5}$ ,  $\rho = 4.0$ ,  $dx = 0.2$ ,  $dt = 0.2$ .  $\theta_{\text{O}}^{\text{min}} \simeq 0.04$ ,  $\theta_{\text{O}}^{\text{max}} \simeq 0.17$ . The broken wavefront is initially 128 cells wide, which is one half the linear size of the integration grid.

on initial conditions, only on the dispersion relation of the medium. As we can see, the selected wavelength in Fig. 13 is much shorter than the front which generates it. On the other hand, the elliptical shape of the spiral again reflects the anisotropy of the Pt(110) surface.

We remark that most of the spirals reported in experiments occurred in situations where the system did not oscillate but behaved instead as an excitable medium. The evolution of spirals under bistable and excitable conditions has been treated elsewhere by a FitzHugh–Nagumo-type model, modified to meet the specific properties of the SPT.<sup>4,42,43</sup>

## V. Discussion

The occurrence of complex spatio-temporal behaviour in the CO + O<sub>2</sub> reaction on Pt(110) has been usually attributed to the effect of gas-phase coupling.<sup>1–3,6,9,17,19</sup> Feedback through the gas-phase is thought to occur *via* small modulations in the CO partial pressure inside the reaction chamber, which are correlated with variations in the total amount of CO adsorbed on the surface and in the rate of CO<sub>2</sub> desorption. Due to the very low pressures and high molecular speeds, the mean free path is larger than the dimension of the vacuum chamber (thus much larger than the size of the sample). Therefore, any pressure variations in the gas-phase equilibrate instantaneously when compared to the relevant time scale of the system, that is, one oscillation period. Sidewise, it was reckoned that spatial coupling alone could never lead to coherent behaviour of the whole surface under oscillatory conditions.

In the effort to access the role of global coupling (GC) in the CO oxidation on Pt(110) several studies were undertaken. In early simulations of cellular automata,<sup>9</sup> rather unrealistic pressure variations had to be applied (~25% of  $p_{\text{CO}}$ , while in experiments these modulations are only about 1–3 %) to realize complete synchronization over the surface, that is, to produce homogeneous oscillations. Subsequent studies<sup>17</sup> relied on the KEE model, supplemented with an equation governing the variations of  $p_{\text{CO}}$  as a function of the integral CO coverage,  $\bar{\theta}_{\text{CO}}$ . Spatial coupling was accounted for by adding a simple Fickian term to the equation governing the amount of adsorbed CO. In numerical simulations of this model, one-dimensional profiles that do resemble standing waves were obtained. However, their wavelength was generally *not intrinsic*, depending on the initial conditions, except in a narrow parameter range. Even so, it is not clear that these standing waves indeed arose because of global coupling since the very same model, but without GC, produced standing-waves with similar characteristics in the close vicinity of the codimensional-two bifurcation Hopf–SNIPER point.<sup>15</sup> Also, in both cases the patterns differ from the standing-wave patterns observed so far in the CO oxidation on Pt(110) in one essential feature: the subharmonic character of the experimentally observed patterns is not reproduced by the KEE model with global coupling which displays instead a 1 : 1 resonance with the global oscillation.

In view of these far from encouraging results, further investigation was based almost exclusively on the Complex Ginzburg–Landau Equation (CGLE), modified to include GC. Underlying this approach is the notion that structured behaviour originates solely from the effect of GC on an oscillatory medium that exhibits the Benjamin–Feir instability, irrespectively of the details of the physical system. Of course, such universal behaviour is only ensured in the neighbourhood of a bifurcation point. In this sense, the normal form approach has a limited scope, being valid close to the line of Hopf bifurcations only. Thus it cannot, for example, account for the relaxation-type oscillations associated with spatio-temporal patterns in the CO + O<sub>2</sub> reaction on Pt(110).

A consistent trend observed in all models relying on GC, either the CGLE or “realistic” models, is that when the strength of the coupling is decreased, amplitude modulations appear, until below a certain threshold value, spatio-temporal chaos sets in. This phenomenon, that has been called the breakdown of global coupling, is thought to characterize generically the transition from regular oscillations to aperiodic behaviour. In this vein, the standing-wave patterns would result from a rather delicate balance between local coupling *via* surface diffusion and global coupling through the gas phase.

For strong enough global coupling, uniform oscillations were obtained in simulations of the CGLE both in one and two dimensions. If the intensity of the coupling is decreased below a certain value, the homogeneous solution becomes unstable with respect to a structured spatio-temporal pattern. Like in our own model, the coherent solution of the CGLE is a superposition of a pure standing wave and a spatially uniform oscillation but displays hexagonal symmetry<sup>19</sup> and a 1 : 1 resonance, contrary to experimental patterns.

It is indisputable that the measured variations in the CO and O<sub>2</sub> partial pressures, despite their small amplitude, do indicate that something on a global scale is happening inside the reacting chamber. Knowing that periodic external forcing can lead to the stabilization of standing waves with respect to other competing spatio-temporal patterns, it would not be surprising if here the standing-wave pattern resulted from that particular kind of self-parametric entrainment.

In a recent publication,<sup>18</sup> von Oertzen *et al.* went back to a “realistic” model formulation with GC. They succeeded in producing standing waves in a five equation variant of the KEE model with Fickian diffusion where, in addition to gas-phase coupling, the influence of subsurface oxygen formation intervenes. Their simulations have shown that a periodic external forcing could stabilize a standing-wave pattern. However, they also found that an *extended* pattern of standing waves never emerged from random initial conditions under the action of *intrinsic* forcing. Moreover, a pre-existing standing-wave pattern would be destroyed by global coupling.

In that model, standing waves only persist when a uniformly oscillating region is taken as the source of global forcing but, clearly, that situation is indistinguishable from strictly external forcing. Thus, the simulations of ref. 18 do not constitute a decisive proof that global coupling is indeed the symmetry-breaking agent. Of course, the ability of gas-phase coupling to synchronize spatio-temporal patterns arising in different parts of the surface is not compromised.

Whether gas-phase coupling is the profound cause or simply the consequence of spatio-temporal pattern formation in the CO oxidation on Pt(110) is a matter that has been intensely debated in the wake of Monte Carlo simulations<sup>20,44</sup> performed over the last few years. Kortlüke and co-workers<sup>20</sup> have questioned the whole idea of global coupling and proposed instead that nucleation phenomena as the underlying reason for globally synchronized oscillations. Their Monte Carlo simulations have failed to reproduce synchronized behaviour when global coupling was taken into account but nucleation processes were neglected. Dense adsorbate islands, with a characteristic length scale much larger than the lattice side length, formed during one oscillation period. This led to the conclusion that homogeneous nucleation phenomena are of paramount importance. Furthermore, domain growth in those cases was strongly reminiscent of the dynamics of phase transitions with non-conserved order parameter, a feature which has been explicitly taken into account in our macroscopic model.

Monte Carlo simulations of the CO + O<sub>2</sub>/Pt(100) and NO + H<sub>2</sub>/Pt(100) reaction systems were also carried out recently by Zhdanov.<sup>44</sup> Although concerned with Pt(100), these studies essentially confirmed the general picture, namely that to achieve synchronization on a global scale it is unneces-



sary to have gas phase coupling once the coupling between adsorbate transport and the surface phase transition is accounted for.

The results of our macroscopic modelling back up the conclusions of the microscopic studies. However, it is also clear that gas-phase coupling may somehow affect the character of spatio-temporal patterns in the CO + O<sub>2</sub>/Pt(110) system. Thus we believe that in order to access the impact of GC, the model should be extended to explicitly include gas-phase coupling. This can be straightforwardly done, by adding a fourth equation accounting for the variation of partial pressure in response to variations in the mean CO surface coverage. Here, the motivation is rather to find out if gas-phase coupling remains strong enough to disturb the stable spatio-temporal patterns that already exist in its absence. It is our opinion that this is indeed the relevant question, all the more since the onset of standing waves, and particularly turbulence, is accompanied by a fall-off in the oscillation amplitudes, necessarily leading to a decline in the efficiency of global coupling.

## VI. Conclusion

The precise role as to the effect of global coupling in the CO oxidation on Pt(110) is still an open question. Contrary to the prevailing thought, we have shown that a model without global coupling gives a better description of the spatio-temporal patterns than models relying on global coupling have so far achieved.

From our point of view, what was missing in a previous attempt<sup>15</sup> and determined its failure, was a comprehensive treatment of mass transport in the presence of the surface phase transition. Merely adding a Fickian diffusion term  $\nabla^2 \theta_{\text{CO}}$  to the kinetic equations gives a poor description of mass transport in this system, because it disregards the interference between surface diffusion and the structural relaxation of the substrate. By including this effect in our model, that is by allowing the topmost layer to participate in the transport of adsorbed CO, we have made spatial coupling much stronger. Sufficiently strong indeed to achieve complete synchronization over the surface (homogeneous oscillations) while promoting spatial symmetry breaking under slightly different conditions. The standing-wave patterns that result have an intrinsic wavelength. They are in good qualitative agreement with the experimentally observed standing waves – both in terms of symmetry as well as in their subharmonic character – and even fine details of the oscillating stripe patterns are reproduced.

Our approach may be extended to other catalytic systems displaying spatio-temporal patterns and oscillations such as CO + O<sub>2</sub>/Pt(100), CO + NO/Pt(100) and NO + H<sub>2</sub>/Rh(110), or adapted to other situations – like, for instance, electrocatalysis<sup>45</sup> – where a phase transition and chemical reactions concur to the formation of nonequilibrium patterns.

## Acknowledgement

P.B. and G.D. acknowledge financial support from the F.N.R.S. (Belgium). J. V. received support from FCT (Portugal).

## References

- R. Imbihl and G. Ertl, *Chem. Rev.*, 1995, **95**, 697.
- S. Jakubith, H. H. Rotermund, W. Engel, A. von Oertzen and G. Ertl, *Phys. Rev. Lett.*, 1990, **65**, 3013.
- H. H. Rotermund, in *Pattern Formation in Continuous and Coupled Systems*, IMA-Series, Springer, New York, 1999, vol. 115, p. 231.
- M. Bär, S. Nettesheim, H. H. Rotermund, M. Eiswirth and G. Ertl, *Phys. Rev. Lett.*, 1995, **74**, 1246.
- H. H. Rotermund, S. Jakubith, A. von Oertzen and G. Ertl, *Phys. Rev. Lett.*, 1991, **66**, 3083.
- K. C. Rose, D. Battogtokh, A. Mikhailov, R. Imbihl and A. M. Bradshaw, *Phys. Rev. Lett.*, 1996, **76**, 3582.
- M. Eiswirth, M. Bär and H. H. Rotermund, *Physica D*, 1995, **84**, 40.
- M. Eiswirth, K. Krischer and G. Ertl, *Surf. Sci.*, 1988, **202**, 565.
- M. Eiswirth, P. Möller, K. Wetzl, R. Imbihl and G. Ertl, *J. Chem. Phys.*, 1988, **90**, 510.
- (a) R. Imbihl, S. Ladas and G. Ertl, *Surf. Sci.*, 1988, **206**, L903; (b) S. Ladas, R. Imbihl and G. Ertl, *Surf. Sci.*, 1988, **198**, 42.
- T. Gritsch, D. Coulman, R. J. Behm and G. Ertl, *Phys. Rev. Lett.*, 1989, **63**, 1086.
- T. Gritsch, D. Coulman, R. J. Behm and G. Ertl, *Appl. Phys. A*, 1989, **49**, 403.
- N. Freyer, M. Kriskinova, G. Pirug and H. P. Bonzel, *Surf. Sci.*, 1986, **166**, 206.
- K. Krischer, M. Eiswirth and G. Ertl, *J. Chem. Phys.*, 1992, **96**, 9161.
- H. Levine and X. Zou, *Phys. Rev. Lett.*, 1992, **69**, 204.
- M. Tammaro and J. W. Evans, *J. Chem. Phys.*, 1996, **104**, 3386.
- (a) M. Falcke and H. Engel, *J. Chem. Phys.*, 1994, **101**, 6255; (b) M. Falcke and H. Engel, *Phys. Rev. E*, 1994, **50**, 1353; (c) M. Falcke, H. Engel and M. Neufeld, *Phys. Rev. E*, 1995, **52**, 763.
- A. von Oertzen, H. H. Rotermund, A. S. Mikhailov and G. Ertl, *J. Phys. Chem. B*, 2000, **104**, 3155.
- D. Lima, D. Battogtokh, A. Mikhailov, P. Borckmans and G. Ertl, *Europhys. Lett.*, 1998, **42**, 631.
- (a) O. Kortlüke, V. N. Kuzovkov and W. von Niessen, *Phys. Rev. Lett.*, 1999, **83**, 3089; (b) O. Kortlüke, V. N. Kuzovkov and W. von Niessen, *J. Chem. Phys.*, 1999, **110**, 11 523; (c) V. N. Kuzovkov, O. Kortlüke and W. von Niessen, *Phys. Rev. Lett.*, 1999, **83**, 1636.
- J. Verdasca, P. Borckmans and G. Dewel, *Phys. Rev. E*, 2001, **64**, 055202 (R).
- V. P. Zhdanov, *Surf. Sci. Lett.*, 1985, **164**, L807.
- S. Ferrer and H. P. Bonzel, *Surf. Sci.*, 1982, **119**, 234.
- R. P. H. Gasser and E. B. Schmidt, *Chem. Phys. Lett.*, 1967, **1**, 457.
- P. C. Hohenberg and B. I. Halperin, *Rev. Mod. Phys.*, 1977, **49**, 435.
- P. Hoffmann, S. R. Bare and D. A. King, *Surf. Sci.*, 1982, **117**, 245.
- J. Verdasca, PhD Thesis, Université Libre de Bruxelles, 2000.
- J. S. Rowlinson and B. Widom, *Molecular Theory of Capillarity*, Clarendon Press, Oxford, 1982.
- R. Gomer, *Rep. Prog. Phys.*, 1990, **53**, 917.
- A. von Oertzen, H. H. Rotermund and S. Nettesheim, *Surf. Sci.*, 1994, **311**, 322.
- (a) B. A. Huberman, *J. Chem. Phys.*, 1976, **65**, 2013; (b) S. Glotzer, D. Stauffer and N. Jan, *Phys. Rev. Lett.*, 1995, **74**, 2034; (c) J. Verdasca, P. Borckmans and G. Dewel, *Phys. Rev. E*, 1995, **52**, R4616.
- (a) A. Onuki, *Phys. Rev. Lett.*, 1982, **48**, 753; (b) M. Joshua, W. I. Goldberg and A. Onuki, *Phys. Rev. Lett.*, 1985, **54**, 1175.
- K. Krischer, M. Eiswirth and G. Ertl, *Surf. Sci.*, 1991, **251/252**, 900.
- A. De Wit, D. Lima, G. Dewel and P. Borckmans, *Phys. Rev. E*, 1996, **54**, 261.
- M. Argentina, P. Couillet and E. Risler, *Phys. Rev. Lett.*, 2001, **86**, 807.
- H. H. Rotermund, *Surf. Sci.*, 1993, **283**, 87.
- H. H. Rotermund, *Surf. Sci.*, 1997, **386**, 10.
- J. Lauterbach, G. Haas, H. H. Rotermund and G. Ertl, *Surf. Sci.*, 1993, **294**, 116.
- K. C. Rose, R. Imbihl, B. Rausenberger, C. S. Rastomjee, W. Engel and A. M. Bradshaw, *Surf. Sci.*, 1996, **352–354**, 258.
- Y. Kuramoto, *Chemical Oscillations, Waves and Turbulence*, Springer, New York, 1984.
- S. Nettesheim, A. von Oertzen, H. H. Rotermund and G. Ertl, *J. Chem. Phys.*, 1993, **98**, 9977.
- M. Bär, N. Gottschalk, M. Eiswirth and G. Ertl, *J. Chem. Phys.*, 1994, **100**, 1202.
- M. Bär and M. Eiswirth, *Phys. Rev. E*, 1993, **48**, R1635.
- (a) V. P. Zhdanov, *Phys. Rev. E*, 1999, **59**, 6292; (b) V. P. Zhdanov, *Phys. Rev. E*, 1999, **60**, 7554.
- (a) Y.-J. Li, J. Osolonovitch, N. Mazouz, F. Plenge, K. Krischer and G. Ertl, *Science*, 2001, **291**, 2395; (b) J. Cristoph, P. Strasser, M. Eiswirth and G. Ertl, *Science*, 1999, **284**, 291.